Water-Stable $DMASnBr_3$ Lead-Free Perovskite for Effective Solar-Driven Photocatalysis

Lidia Romani,[a] Andrea Speltini,[b] Francesco Ambrosio,[c,d,] Edoardo Mosconi,[c] Antonella Profumo,[a] Marcello Marelli,[h] Serena Margadonna,[f] Antonella Milella,[g] Francesco Fracassi,[g] Andrea Listorti,[g] Filippo De Angelis,[c,e] Lorenzo Malavasi[a,*]*

[a]Department of Chemistry and INSTM, University of Pavia,Via Taramelli 16, Pavia, 27100, Italy

[b]Department of Drug Sciences, University of Pavia, Via Taramelli 12, Pavia, 27100, Italy

[c]Computational Laboratory for Hybrid/Organic Photovoltaics (CLHYO), Istituto CNR di Scienze e Tecnologie Chimiche "Giulio Natta" (CNR-SCITEC), Via Elce di Sotto 8, 06123 Perugia, Italy

[d]CompuNet, Istituto Italiano di Tecnologia, Via Morego 30, 16163 Genova, Italy

[e]Department of Chemistry, Biology and Biotechnology, University of Perugia, Via Elce di Sotto 8, 06123 Perugia, Italy

[f]Materials Research Centre and SPECIFIC, College of Engineering, Swansea University, SA1 8EN Swansea, U.K.

[g]Department of Chemistry, University of Bari, Via Orabona 4, Bari, 70126, Italy

[h]National Research Council, CNR-SCITEC, Via G. Fantoli 16/15, 20138 Milan, Italy

Corresponding Authors

Francesco Ambrosio, email: francesco.ambrosio@iit.it; Lorenzo Malavasi, email: lorenzo.malavasi@unipv.it; tel. +39 382 987921

ABSTRACT

Water-stable metal halide perovskites could foster tremendous progresses in several research fields where their superior optical properties can make differences. In this work we report clear evidence of water stability in a lead-free metal halide perovskite, namely $DMASnBr_3$, obtained by means of diffraction, optical and x-ray photoelectron spectroscopy. Such unprecedented water-stability has been applied to promote photocatalysis in aqueous medium, in particular by devising a novel composite material by coupling $DMASnBr_3$ to g-C_3N_4, taking advantage from the combination of their optimal photophysical properties. The prepared composites provide an impressive hydrogen evolution rate >1700 μmol g^{-1} h^{-1} generated by the synergistic activity of the two composite costituents. DFT calculations provide insight into this enhancement deriving it from the favorable alignment of interfacial energy levels of $DMASnBr_3$ and g-C_3N_4. The demonstration of an efficient photocatalytic activity for a composite based on lead-free metal halide perovskite in water paves the way to a new class of light-driven catalysts working in aqueous environments.

TABLE OF CONTENTS GRAPHICS

Exceptionaly water-stability has been confirmed in DMASnBr3 and exploited in photocatalysis to enhance the hydrogen photogeneration of graphitic carbon nitride.

Introduction

Metal halide perovskites (MHPs) semiconductors possess unique optical properties, such as high optical absorption in the visible region, tunable band-gap and long carrier lifetime, which have been extensively exploited in photovoltaics and optoelectronic applications.[1] More recently there has been a growing interests towards novel applications of MHPs, in particular in the field of solar-driven photocatalysis.[2] Compared to traditional metal oxide photocatalysts, MHPs possess relatively narrow bandgaps, allowing the absorption of low-energy photons.[2] In addition, the electronic band structure of many perovskites places their band edges in excellent positions to perform hydrogen photogeneration and carbon dioxide photoreduction.[2] However, some of the most interesting photocatalytic reactions such as H_2O splitting, CO_2 and N_2 reduction, dye degradation, require the use of water or alternative polar solvents, this represent a conundrum foreseeing MHPs utilization. It is well known, in fact, that MHPs are highly unstable upon moisture and water exposure, therefore those media are hardly compatible with most of the current known MHPs.[2-4] Due to these constrains, the demonstration of hydrogen photogeneration by using $MAPbI_3$, has been only possible in dynamic equilibrium with aqueous hydrogen iodide (HI).[5-8] In addition to the use of saturated halo acids, other strategies to overcome the water-instability of MHPs consider the use of low-polarity solvents and encapsulation strategies.[2] These last approaches have been used, for example, in several photocatalytic organic syntheses, such C–C, C–N and C–O bond-formations, another very exciting field where the photophysical properties of MHPs could provide unprecedented opportunities to researches.[9] Clearly, the possibility of employing MHPs as photocatalysts and co-catalysts, in photocatalytic reactions in aqueous environment, could open an unprecedented novel field of applications, which can take advantage of their superior, as well as highly tunable, electronic properties.

Triggered by the aforementioned opportunities, growing interest for water-stable MHPs is fostering current research. Materials such as $DMASnX_3$ (DMA=dimethylammonium, X=Br and I) family, have shown an impressive stability when immersed in water, as confirmed by the collection of the diffraction patterns before and after water interaction.[10,11] In these reports, the MHPs do not dissolve in water but it rather remain dispersed in solution, maintaining unchanged the crystal structure and the optical properties. [10,11] The precise origin of the superior stability of these phases is not yet known, but it could be related to the relatively high hydrophobic nature of the dimethylammonium cation. Both $DMASnBr_3$ and $DMASnI_3$ systems owing to their exceptional water stability call for potential eco-friendly applications and so they have been used as photocatalyst for H_2 evolution in deionized water rather than in saturated hydroiodic acid (HI) solution, with a H_2 evolution rate of about 1 ($DMASnBr_3$) and 0.6 ($DMASnI_3$) $\mu mol\ h^{-1}g^{-1}$ and with good recycling properties.[10,11]

Another example of water stable perovskite material has been recently reported, $C_{22}H_{18}N_2(PbI_3)_2$ perovskite an efficient active material for photovoltaic applications, was monitored through X-ray powder diffraction carried out after prolonged water immersion at room temperature.[12] Unlike the methylammonium counterpart, this MHP proved to be unaffected by water exposure. In this case, the authors indicate that the lack of reactivity towards water could be attributed to the quaternary nature of the nitrogen atoms present in the organic units.[12] In addition, hydroxyl ammonium lead iodo-chloride, $OHNH_3PbI_2Cl$ and hydroxyl ammonium lead chloride, $OHNH_3PbCl_3$ materials showed to be water-stable for 45 days.[13] Some of us also recently reported an extremely high stability of two-dimensional (2D) lead-free perovskites based on phenylethylammonium (PEA), namely PEA_2SnBr_4, which, as well, does not dissolve in water (but disperse) and which structural and optical properties remain unchanged after water treatments.[14] For 2D perovskites some computational work is addressing such improved water stability, showing also that the same mechanism is thought to protect tin from +2 to +4 oxidation.[15] Finally, very recently, a novel 1D hybrid tin iodide

material, namely (DAO)Sn_2I_6(DAO, 1,8-octyldiammonium), has shown to emit broad light with high quantum efficiency and stability in water for more than 15 hours.[16]

Focusing on the photocatalytic hydrogen generation, except for the $DMASnX_3$ compositions cited above, the use of MHPs in dynamic equilibrium with aqueous halo acids does not appear to be a practical solution, as it requires the presence of high amounts of HX to avoid perovskite degradation and, in addition, the use of lead-based soluble perovskites precursors may be environmental hazardous due to possible lead contamination.

Motivated by the above considerations, we decided to afford a more detailed study on $DMASnBr_3$ MHP exploitation in photocatalysis.[10] In order to improve the Hydrogen Evolution Reaction (HER) performance of $DMASnBr_3$, we devised a novel approach based on the synthesis of composites between the MHP and a well-known visible light photocatalyst, namely graphitic carbon nitride, g-C_3N_4.

Polymeric carbon nitride, g-C_3N_4, has become the state-of-the-art photocatalyst under visible-light, featuring a relatively narrow band gap (ca. 2.7 eV) and conduction and valence band positions suitable to run relevant oxidation and reduction processes.[17,18] To further improve the properties of individual g-C_3N_4, in particular to increase charge migration and recombination time, and to extend the absorption range, significant research has been devoted to the preparation of g-C_3N_4 composites with metals, bimetals, semiconductors (oxides, sulfides, and the like), graphene, carbon dots, conductive polymers, sensitizers, among others, showing a promising improvement of the HER.[19-21] Based on the these reports, we performed an investigation of the possible use of the $DMASnBr_3$ perovskite as an efficient co-catalysts for carbon nitride, trying to exploit its beneficial and superior optical properties and taking advantage of preliminary evidences of water-stability of this and related materials.[10,11]

Before addressing the use of $DMASnBr_3$ in photocatalysis, we further elaborated on its water-stability.

Figure 1a shows a sketch of the $DMASnBr_3$ crystal structure, characterized by distorted edge-sharing $SnBr_6$ octahedra, while Figure 1b reports the x-ray diffraction pattern of a sample prepared by mechanochemical synthesis (1b, as prep top line), starting from DMABr and $SnBr_2$ milled at 300 rpm for 12 hours (see the Supporting Information, SI), confirming the expected orthorhombic structure (*Pbca*) reported as reference pattern in the figure (vertical red bars), thus indicating that ball-milling is a good synthetic strategy also for Sn-based perovskites.[22,23]

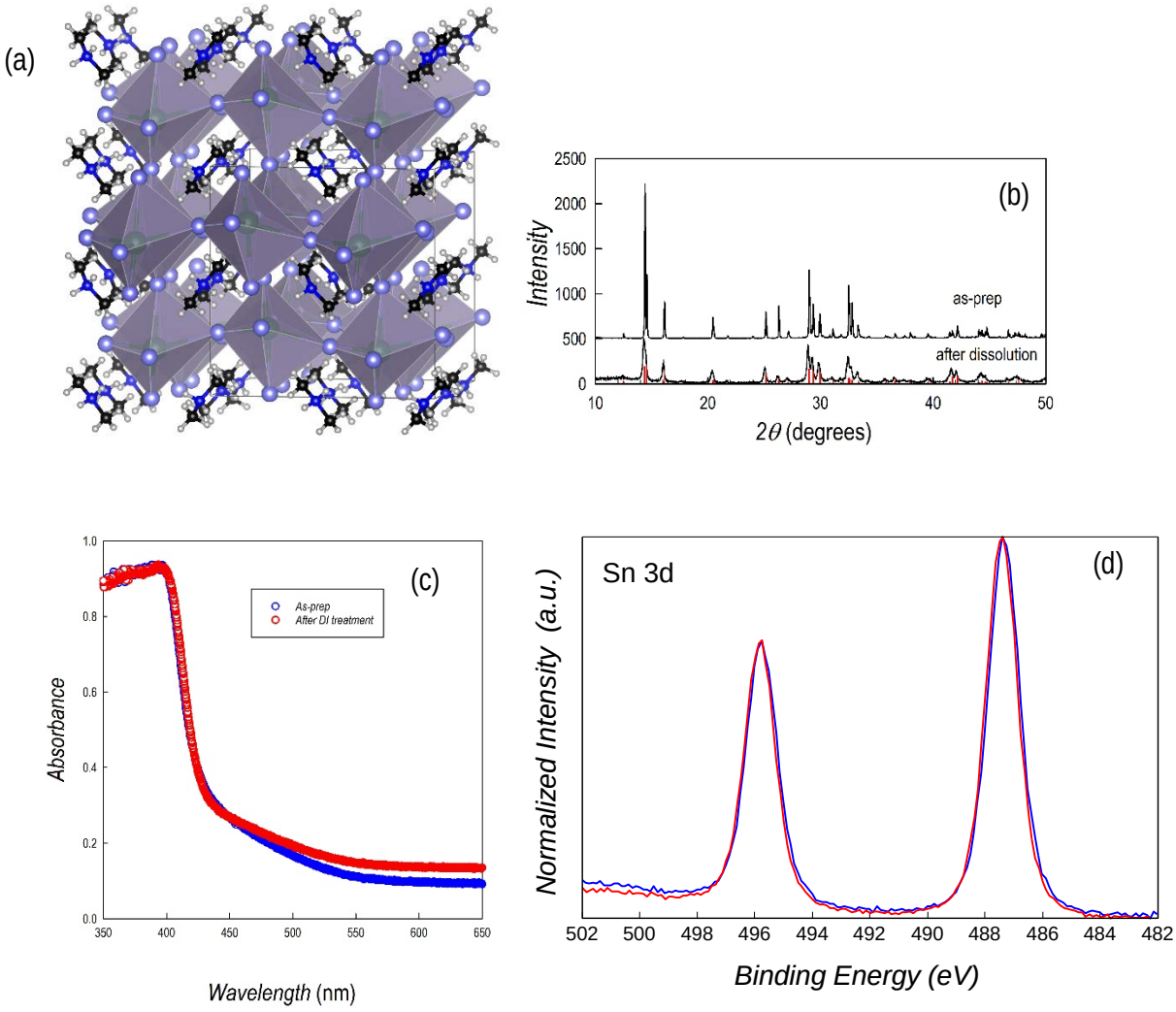

Figure 1. (a) Schematic representation of $DMASnBr_3$ crystal structures; (b) XRD pattern of $DMASnBr_3$ synthesized by ball-milling where red vertical bars refer to the reflection positions for orthorhombic structure of the perovskite (*Pbca*): top pattern: as-prepared material; bottom pattern: after recovery from aqueous solution; (c) UV-Vis spectra of as-synthesized $DMASnBr_3$ (blue) and after recovery from aqueous solution (red); (d) Sn 3d XPS spectra of as-synthesized $DMASnBr_3$ (blue) and after recovery from aqueous solution (red).

Water-stability of the perovskite has been checked by suspending it in deionized water (DW), followed by stirring for 4 hours and then filtering. By visual inspection, suspended powders are clearly visible in the aqueous phase. The recovered powder underwent XRD, shown in Figure 1b, bottom line, and, as it can be clearly appreciated by comparison with Figure 1b, top line, the material kept its original crystal structure. As a further proof of structural stability, we tested the potential leaching of Sn in water by determining, with ICP-OES analysis, the amount of tin contained in the water where the perovskite had been suspended under stirring for 4 hours. The analysis demonstrates that less than 0.5% of the starting Sn, based on the amount of Sn in the starting suspended powder, is released from the MHP in water after this stirring time. Time-dependent release study up to 32 hours, under the same experimental conditions, confirmed the perovskite water-stability, by showing a maximum Sn release of about 5% (plateau value) after this prolonged soaking (see Figure S1). In addition, Figure 1c compares the UV-Vis spectrum of the as-prepared $DMASnBr_3$ with the spectrum of the sample after being treated in DW, confirming that the optical properties as well are unaltered by the water treatment. Finally, a further and definitive confirmation of the water-stability of $DMASnBr_3$ was obtained by X-ray Photoelectron Spectroscopy (XPS). Figure 1d reports the Sn 3d spectra of the as-prepared sample (blue curve) and of the sample after water treatment (red line): the perfectly overlapping spectra, with unchanged peak shape and position (Sn $3d_{5/2}$ at 487.3 eV), clearly demonstrate that our material is stable under water treatment, also confirming the +2 oxidation state of Sn state without any evidence of sample oxidation.[24] All these evidences provide a solid and unambiguous proof of water stability of $DMASnBr_3$.

After having assessed and clearly demonstrated the exceptional water-stability of $DMASnBr_3$, we report in the following the first successful preparation of $DMASnBr_3$@g-C_3N_4 composites at different MHP loadings ranging from 1 to 33 wt%. The samples have been prepared by means of mechanochemistry starting from mixtures of DMABr, $SnBr_2$ and g-C_3N_4 (synthesized from dicyandiamide decomposition at 600 °C in N_2 flux) and their crystal structure

characterized by laboratory X-ray diffraction (more details in the SI). A schematic representation of the structure of g-C_3N_4 is reported in Figure 2a and characterized by the tri-s-triazine ring structure, which is connected by the N atoms to form a p-conjugated polymeric network. Figures 2b reports the XRD pattern of the pristine g-C_3N_4 materials, while Figure 2c reports some selected patterns of the $DMASnBr_3$@g-C_3N_4 composites at varying wt% of MHP loading relative to g-C_3N_4.

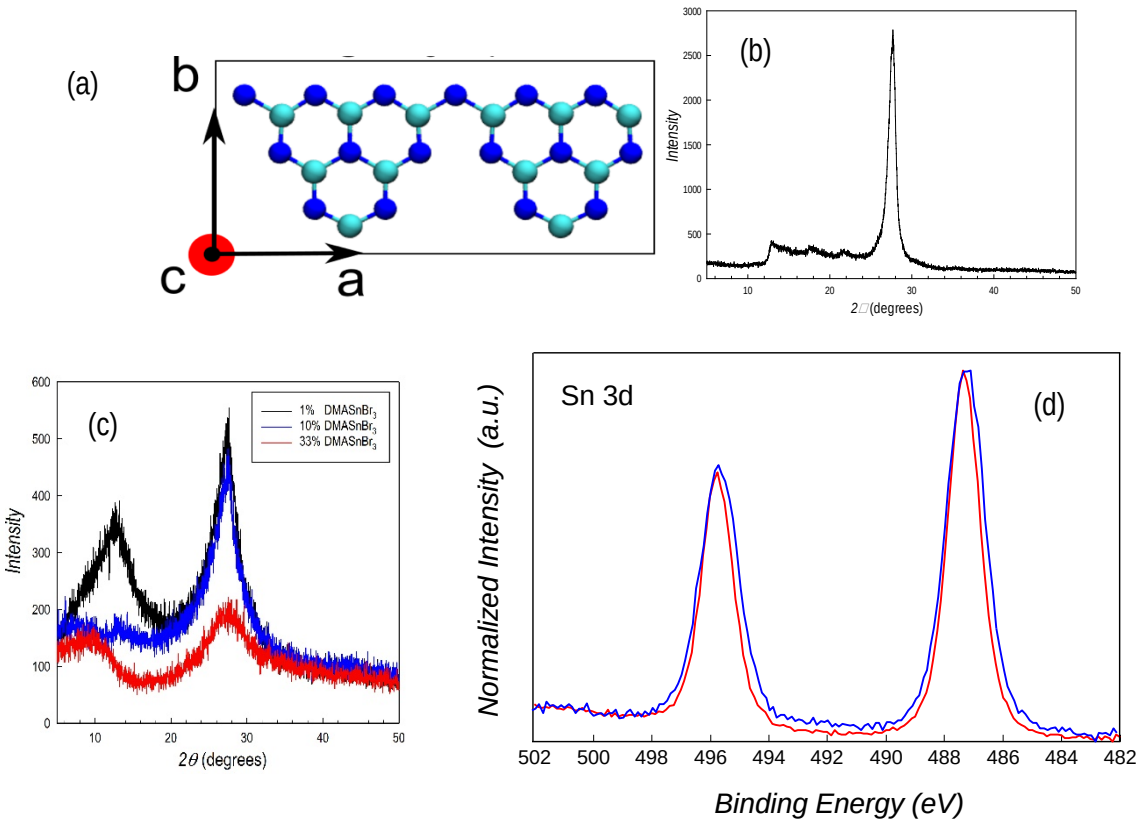

Figure 2. (a) Schematic representation of g-C_3N_4; (b) XRD pattern of starting g-C_3N_4 prepared from thermal condensation of dicyandiamide at 600°C in nitrogen flux; (c) XRD patterns of $DMASnBr_3$@g-C_3N_4 composites at different percentages of metal halide perovskite loading; (d) Sn 3d XPS spectra of $DMASnBr_3$ (red curve) and of $DMASnBr_3$@g-C_3N_4 composite at 33wt% (blue curve).

Figure 2c shows that composites have an overall amorphous-like structure, with the main peak of g-C_3N_4 around 28° and the general sample scattering becoming progressively less intense with the increase of the amount of metal halide perovskite (compare also with Figure 2b of pure g-C_3N_4). No clear diffraction peaks of crystalline perovskites are found in the

patterns, suggesting that the presence of g-C_3N_4 during ball-milling tends to reduce the structural order of the $DMASnBr_3$. FT-IR data (Figure 2 of SI) indicate the presence of the metal halide perovskite thorough specific fingerprint regions of the $DMASnBr_3$ in the composite. However, a more conclusive information regarding the presence of the MHP in the composite was obtained by XPS analysis, carried out on the $DMASnBr_3$@g-C_3N_4 composite at 33wt% loading, which is the most active one (see later in the text). Figure 2d compares the Sn 3d XPS spectrum of pristine $DMASnBr_3$ with that of the $DMASnBr_3$@g-C_3N_4 composite, showing the same peak position and shape. In addition, N1s XPS spectra confirms the presence of the typical fingerprint of ammonium group (401.4 eV) in the composite and its absence in the pristine g-C_3N_4 (Figure S3).[25,26] These results rule out also the possible decomposition of the perovskite into the composite since this would lead to changes of the binding energies in the Sn spectra, which is not the case as clearly shown in Figure 2d. Scanning Electron Microscopy (SEM) and EDX analysis of composites are shown in Figure S4, indicating a morphology without distinct features, as anticipated due to ball-milling process, and micron-sized grains. The Br/Sn ratio determined over a large scanning area (Figure S4f) is in fairly good agreement with nominal value. Finally, Scanning Transmission Electron microscopy (STEM) of the composites along with EDX data (on a smaller area of about 1 μm), further substantially confirm the composition and the local homogeneous distribution of the elements (i.e. Br, Sn, C and N - FigureS5).

Optical absorbance spectra of $DMASnBr_3$@g-C_3N_4 composites (15 and 33wt%) (Figure 3a,b) show a slight blue-shift with respect to g-C_3N_4 by increasing the amount of $DMASnBr_3$ with the band gap (calculated from the Tauc plots of Figure 3b) varying from ~2.7 eV (for pure carbon nitride) to ~2.85 eV, without significant differences among the composites at the various perovskite loadings. This result could be anticipated considering the relatively small difference in the band-gap between carbon nitride and $DMASnBr_3$.

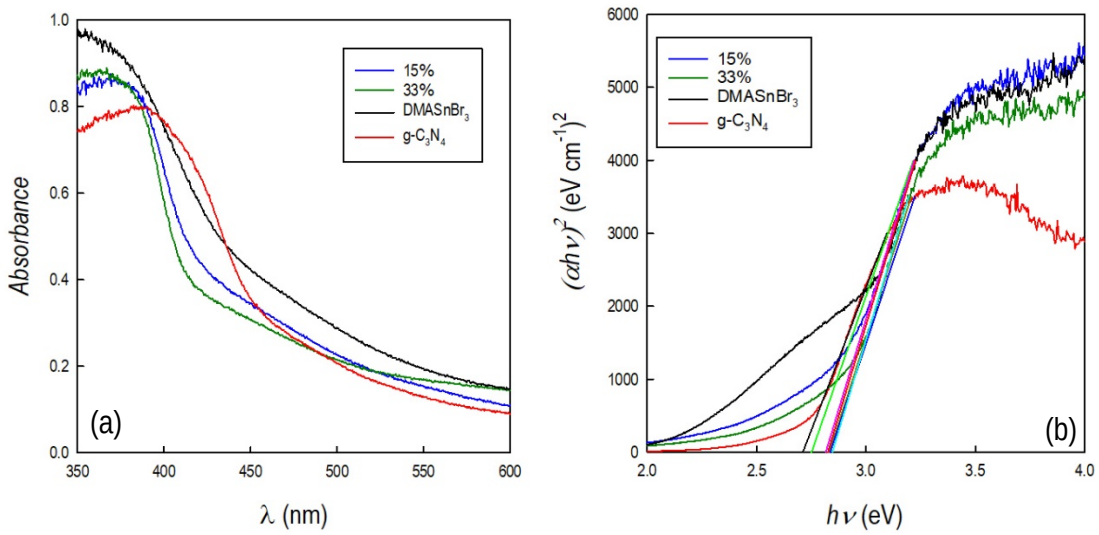

Figure 3. (a) Absorption spectra and (b) Tauc plots of $DMASnBr_3$@g-C_3N_4 composites at different percentages of MHP loading. g-C_3N_4 refers to pristine carbon nitride.

Surface area of selected representative samples has been measured by B.E.T method and the results are listed in the SI (Table S1). g-C_3N_4 synthesized from DCD condensation at 600 °C shows, as expected, the highest surface area (around 26 m^2/g). In general, there is a trend towards lower values by increasing the loading of the MHP during the ball-milling process. Such synthetic route, while favoring the dispersion and improving the contact between the two materials, leads to a reduction of the surface area in the samples.[27-29] However, ball-milling is a very simple and straightforward synthetic method which is suitable also to large scale catalyst synthesis and its positive effect on the HER rate of g-C_3N_4-based composites has been already observed.[27-29]

We determined the hydrogen photogeneration characteristics of the above discussed composites by employing common protocols used for similar g-C_3N_4-based composites.[17] The results reported in the following have been performed on several replicas of the composites and the experimental details of the hydrogen evolution tests are reported in the Experimental Section. Firstly, hydrogen photogeneration properties of the $DMASnBr_3$@g-C_3N_4 composite have been determined in 10% (v/v) aqueous triethanolamine (TEOA) as a typical sacrificial

agent, and without any metal co-catalyst (*e.g.* Pt). The HERs as a function of perovskite loading of the composites are shown in Figure 4.

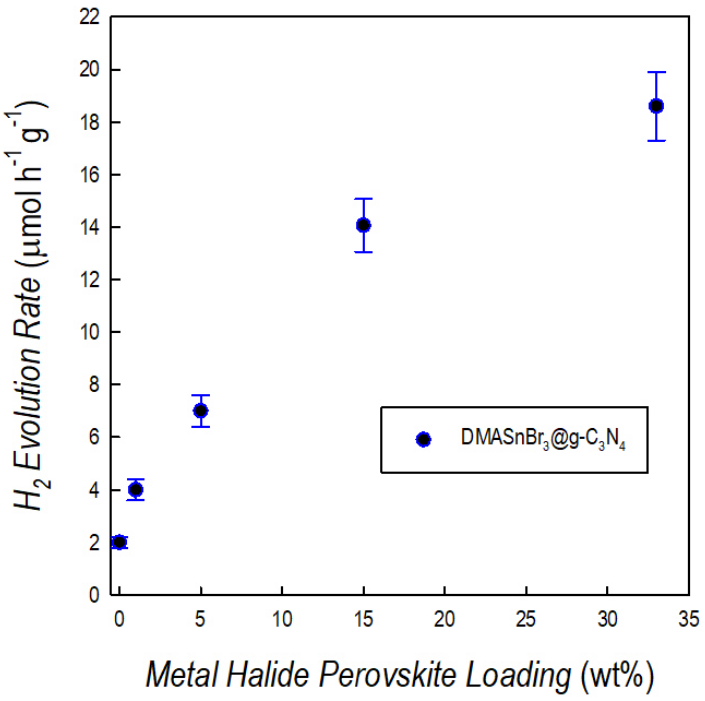

Figure 4. Hydrogen evolution rates for $DMASnBr_3$@g-C_3N_4 composites (1 g L^{-1}) at different percentages of MHP loading in 10% (v/v) TEOA aqueous solution and without any metal co-catalyst, under simulated solar light (6 h irradiation, Xenon lamp, 500 W m^{-2}, 300-800 nm, IR-treated soda lime glass UV outdoor filter). RSD < 10% (*n*=3).

The composites perform significantly better than g-C_3N_4 alone, even for small perovskite amounts (1 wt%) (see Table 1), and the highest HER for the composite (~19 µmol g^{-1} h^{-1}) represents a nearly 10-fold improvement with respect to pure g-C_3N_4 (~2 µmol g^{-1} h^{-1} – 0% MHP loading in Figure 4). Irradiation of TEOA aqueous solution (no catalyst, blank control test) yielded just 0.014 µmol per hour, confirming the key role of each catalyst. Such 10-fold improvement for the composites H_2 evolution is even more significant if considering that their surface area is, *e.g.* at 33% loading, 1/7 of that of g-C_3N_4 (see Table S1) and that such parameter strongly affects the photocatalytic performances of carbon nitride (as a rough idea, in our

previous experiments on g-C_3N_4, we demonstrated that a reduction of 1/5 of the surface area correspond to about 1/3 reduction of hydrogen photogeneration).[30] Moreover, this is an impressive value also considering the absence of any metal co-catalyst, which is usually employed with g-C_3N_4 and/or common semiconducting photocatalysts. Optimal photocatalytic performance has been found at 33wt% MHP. Furhter loading (e.g. 50%, data not shown) did not provide any enhancement in the hydrogen photogeneration while a general reduction (below about 14 μmol g^{-1} h^{-1}) was observed possibly due to covering of active sites and/or shielding of light absorption in g-C_3N_4.

To clarify the role of surface area and to provide comparable data, we performed an experiment with a lower amount of g-C_3N_4 (0.13 g L^{-1}) which corresponds to approximately the same catalytic surface in suspension for 1 g L^{-1} of 33 wt% $DMASnBr_3$@g-C_3N_4 (see Table S1). Under this conditions, the irradiation test gave little H_2 (0.5 μmol g^{-1} h^{-1}), far below the HER of the composite material (see Figure 4).

Notably, there is a clear synergic role within the composite since, under the same experimental conditions, g-C_3N_4 produces 2 μmol g^{-1} h^{-1} while $DMASnBr_3$ stands below 1 μmol g^{-1} h^{-1}.[10] The results reported so far are the first clear evidence of efficient carbon nitride/lead free MHP composites which can promote hydrogen evolution from aqueous solution without the need of any hydrogen halide (*e.g.*, HI).

Photogeneration experiments have been further undertaken employing metallic Pt as co-catalyst (3 wt%), to reproduce the common photocatalytic conditions used for carbon nitride-based composites.[1-5] Under these conditions, the $DMASnBr_3$@g-C_3N_4 with 33wt% MHP composite reached an impressive H_2 production of 1730 μmol g^{-1} h^{-1} (apparent quantum yield, AQY 6.6%) that places it close to the materials with ultra-high HER.[18] We stress that such performance is achieved with a composite presenting a quite low surface area (below 4 m^2 g^{-1}, Table S1), thus leaving plenty of space to the employment of mesoporous and/or nanocrystal

based analogous composites which may achieve even higher photogeneration rates. Also under these experimental conditions (*i.e.*, with Pt co-catalyst), a real synergic effect of the composite is evident, being the HER of g-C_3N_4 620 μmol g^{-1} h^{-1} (for a surface area 7-fold higher than the composite) and that of $DMASnBr_3$ around 6 μmol g^{-1} h^{-1}.[18] The kinetics of H_2 evolution for the composite was also studied and the profile (Figure 5) indicates substantially a linear increase of the production as function of time.

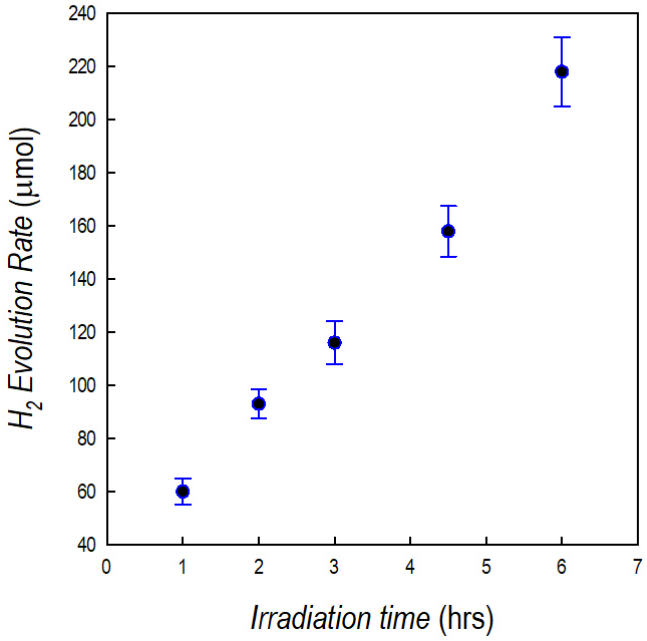

Figure 5. Hydrogen evolution profile over irradiation time for the 33wt% $DMASnBr_3$@g-C_3N_4 composite (1 g L^{-1}, 10% v/v TEOA, 3 wt% Pt), under simulated solar light (Xenon lamp, 500 W m^{-2}, 300-800 nm, IR-treated soda lime glass UV outdoor filter). RSD < 10% (*n*=3).

For comparison with a benchmark catalyst, the well-known Evonik AEROXIDE® P25 TiO_2 (10-50 nm, 60.8 m^2 g^{-1}) was tested (1 g L^{-1}, 10% v/v TEOA, 6 h irradiation). Despite its 15-folds higher surface area, the commercial semiconductor gave HERs of 155 and 6970 μmol g^{-1} h^{-1}, without and with 3% Pt, correspondingly, further corroborating the above discussion.

To assess the effect of the sacrificial agent, the 33wt% MHP composite was tested also in pure water, obtaining a hydrogen production of 14 μmol g^{-1} h^{-1} (7 μmol g^{-1} h^{-1} with no metal co-catalyst, to be compared to a H_2 production < 0.1 μmol g^{-1} h^{-1}, using g-C_3N_4 alone, see Table 1).

A final test to prove the effectiveness of $DMASnBr_3$@g-C_3N_4 (33wt% perovskite) foreasaid its photogeneration activity in 0.1 M aqueous glucose, representative of a biomass-derived sacrificial agent. The HER activity for $DMASnBr_3$@g-C_3N_4 (3wt% Pt) was 300 μmol g^{-1} h^{-1} (AQY 1.1%) while that of g-C_3N_4 was 3 μmol g^{-1} h^{-1}, resulting in an impressive 100-fold improvement. Meanwhile in absence of Pt, the composite produced 8 μmol g^{-1} h^{-1} of hydrogen gas with carbon nitride alone resulted in not quantifiable H_2 (< 0.4 μmol g^{-1} h^{-1}). In the absence of any catalyst, irradiation of glucose solution yielded not quantifiable H_2 evolution (< 0.01 μmol per hour). A summary of the HERs for different composite compositions and photogeneration conditions is reported in Table 1.

Table 1. HERs for g-C_3N_4 and $DMASnBr_3$@g-C_3N_4 composites at different percentages of metal halide perovskite loading as well as for $DMASnBr_3$@g-C_3N_4 33% under different photocatalysis test conditions. RSD < 10% (*n*=3).

Catalyst	**Experimental Conditions**	**HER (μmol g^{-1} h^{-1})**
g-C_3N_4	Pure water, no Pt	< 0.1
g-C_3N_4	10% (v/v) TEOA, no Pt	2.0
1% $DMASnBr_3$@g-C_3N_4	10% (v/v) TEOA, no Pt	4.0
5% $DMASnBr_3$@g-C_3N_4	10% (v/v) TEOA, no Pt	7.0
15% $DMASnBr_3$@g-C_3N_4	10% (v/v) TEOA, no Pt	14.1
33% $DMASnBr_3$@g-C_3N_4	10% (v/v) TEOA, no Pt	18.6
33% $DMASnBr_3$@g-C_3N_4	Pure water, no Pt	7.0

33% $DMASnBr_3$@g-C_3N_4	Pure water, 3 wt% Pt	14.0
g-C_3N_4	10% (v/v) TEOA, 3 wt% Pt	620
$DMASnBr_3$	10% (v/v) TEOA, Pt 3 wt%	6
33% $DMASnBr_3$@g-C_3N_4	10% (v/v) TEOA, Pt 3 wt%	1730
g-C_3N_4	0.1 M aqueous glucose, no Pt	< 0.4
g-C_3N_4	0.1 M aqueous glucose, Pt 3 wt%	3
33% $DMASnBr_3$@g-C_3N_4	0.1 M aqueous glucose, no Pt	8
33% $DMASnBr_3$@g-C_3N_4	0.1 M aqueous glucose, Pt 3 wt%	300

Finally, to test the integrity of the spent catalyst, XRD has been collected after the photogeneration reaction on the $DMASnBr_3$@g-C_3N_4 (33wt%) showing a pattern in very good agreement with that reported in Figure 2c (see Figure S6).

These striking results can be interpreted by considering the alignment of the relevant energy levels at the semiconductor-water interface. We employed advanced electronic-structure calculations (see Experimental Section, Refs. 31, 32 and Figures S7-S9) to align the band edges of $DMASnBr_3$ and g-C_3N_4 with respect to a computational standard hydrogen electrode via the vacuum level.[33,34]

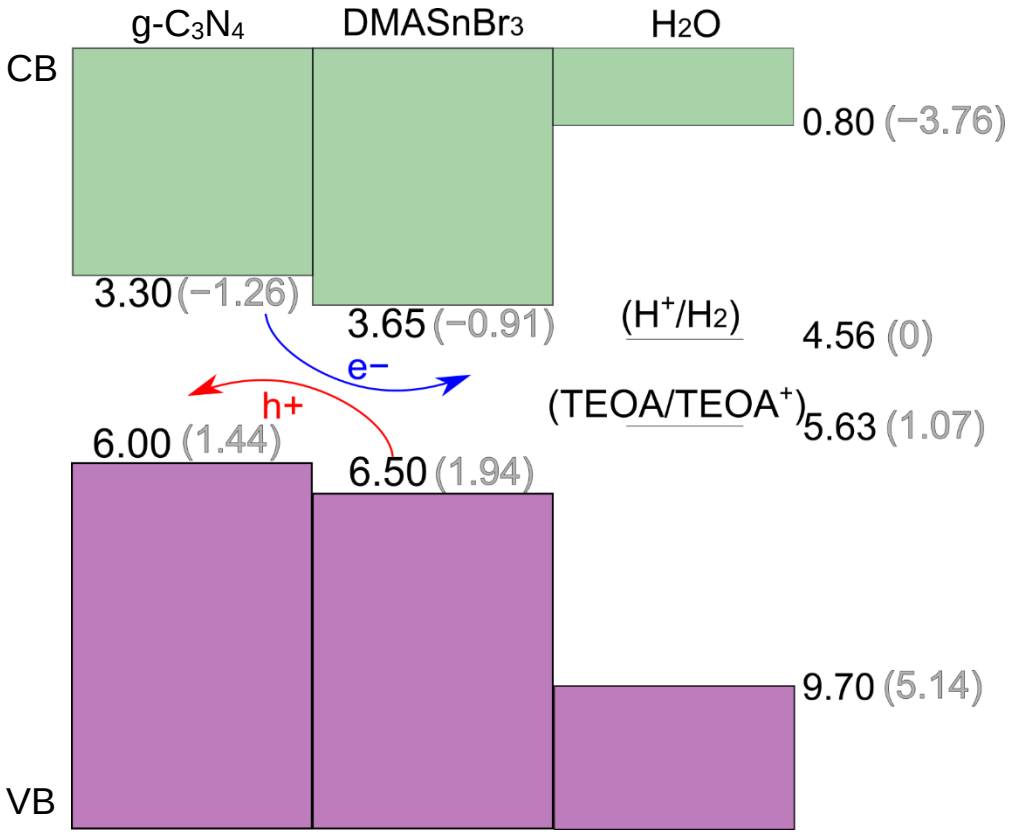

Figure 6. Valence band (VB) and conduction band (CB) edges of g-C_3N_4 and $DMASnBr_3$ aligned with the band edges of liquid water and with the H^+/H_2 and TEOA/TEOA+ redox level (cf. Ref. 36) through the vacuum level. Values are referred to the vacuum level (black) and to the standard hydrogen electrode (SHE, grey) using the computatational alignment achieved in Ref. 34. All values are given in eV.

The results depicted in Figure 6 show that valence and conduction band edges of $DMASnBr_3$ (g-C_3N_4) are placed at 6.5 (6.0) and 3.65 (3.3) eV below the vacuum level, respectively (in parentheses are reported the corresponding values referred to SHE). Being both materials absorbers in the visible region, the achieved alignment implies that that excited electrons in the conduction band of g-C_3N_4 can be effectively transferred to the perovskite. Similarly, holes in the valence band of $DMASnBr_3$ can migrate to the g-C_3N_4. Overall, this alignment results in an efficient separation and transport of photo-induced electrons and holes, which is likely to drastically hinder charge recombination. Furthermore, since the rate of non-adiabatic charge transfer shows an inverse exponential dependence on the energy difference between initial and final state, the lower energy difference between the conduction band edge

of $DMASnBr_3$ and the H^+/H_2 produces a kinetically more favorable alignment.[35] We notice that, for the same reason, the alignment between the valence band of g-C_3N_4 and the TEOA/$TEOA^+$ redox level (cf. Figure 6) would be particularly beneficial for the oxidation reaction. Overall, the mechanism of hydrogen photogeneration reaction in this novel composite could be thought to be analogous to previous Z-scheme photocatalysis heterojunction systems found in g-C_3N_4 composites providing an efficient charge separation and improved photocatalysis.[19]

Conclusions

In summary, we reported clear and solid evidences of superior water stability for $DMASnBr_3$ perovskite. Such excellent properties have been exploited in the design and realization of a new class of photocatalytic composites based on the coupling between g-C_3N_4 and $DMASnBr_3$, showing excellent catalytic properties in aqueous solutions under simulated solar light. The results show a record HER rate > 1700 μmol g^{-1} h^{-1} for the best performing composite also highlighting an effective synergic role between the perovskite and the carbon nitride deriving from a beneficial band alignment as demonstrated by DFT calculations. Their use has been also verified in water containing glucose, as model water-soluble sacrificial biomass, resulting in an impressive 100-fold improvement with respect to bare g-C_3N_4 in the hydrogen generation for the composite. Moreover, leaching tests along with XPS measurements confirmed the insolubility of the $DMASnBr_3$ perovskite.

These preliminary results pave the way to the realization of a complete new class of photocatalysts which couple the efficient optical absorption and carrier lifetime properties of MHPs with the well-known photocatalytic activity of carbon nitride. With the advancement of materials discovery in the field of perovskites, several low-dimensional and possibly lead-free compounds are expected to be sufficiently stable in aqueous solution to be explored as potential catalysts. In addition, further research can extend the present concept to meso- and/or nanostructured composites thus further improving on the here reported HER performance.

Supporting Information

Supporting Information Available: FT-IR spectra, Scanning and Transmission Electron Microscopy results, additional XRD data, additional XPS spectra, surface are data, graphical representation of the supercells used for the computational work. Experimental and computational details.

Acknowledgement

FA, EM and FDA acknowledge support from the Ministero Istruzione dell'Università e della Ricerca (MIUR) and the University of Perugia through the program "Dipartimenti di Eccellenza 2018-2022" (grant AMIS) and from the European Union's Horizon 2020 research and innovation programme under Grant Agreement No 764047 of the Espresso project." LM acknowledge financial support from R.S.E. SpA (Ricerca sul Sistema Energetico). We acknowledge prof. Chiara Milanese for FT-IR data acquisition and analysis.

References

[1] S. D. Stanks, H. L. Snaith, *Nature Nanotec.* **2015**, *10*, 931-402.

[2] H. Huang, B. Pradhan, J. Hofkens, M. B. Roeffaers, J. A. Steele, *ACS Energy Letters* **2020**, *5*, 1107-1123.

[3] C. Zheng, O. Ruberl, *J. Phys. Chem. C* **2019**, *123*, 19385-19394.

[4] J. A. Christians, P. A. Miranda Herrera, P. V. Kamat, *J. Am. Chem. Soc.* **2015**, *137*, 1530–1538.

[5] Z. Zhao, J. Wu, Y.-Z. Zheng, N. Li, X. Li, X. Tao, *ACS Catal.* **2019**, *9*, 8144-8152.

[6] S. Park, W. J. Chang, C. W. Lee, S. Park, H.-Y. Ahn, K. T. Nam, *Nature Energy* **2016**, *2*, 16185.

[7] M. Wang, Y. Zuo, J. Wang, Y. Wang, X. Shen, B. Qiu, L. Cai, F. Zhou, S. P. Lau, Y. Chai, *Adv. Energy Mater* **2019**, *9*, 1901801.

[8] Z. Zhao, J. Wu, Y.-Z. Zheng, N. Li, X. Li, Z. Ye, S. Lu, X. Tao, C. Chen, *Appl. Catal. B* **2019**, *253*, 41-48.

[9] X. Zhu, Y. Lin, J. San Martin, Y. Sun, D. Zhu, Y. Yan, *Nat. Commun.* **2019**, *10*, 2843,

[10] A. Pisanu, A. Speltini, P. Quadrelli, G. Drera, L. Sangaletti, L. Malavasi, *J. Mater. Chem. C* **2019**, *7*, 7020.

[11] D. Ju, X. Zheng, J. Liu, Y. Chen, J. Zhang, B. Cao, H. Xiao, O. F. Mohammed, O. M. Bakr, X. Tao, *Angew. Chem., Int. Ed.* **2018**, *57*, 14868-14872.

[12] A. Latini, S. Quaranta, F. Menchini, N. Lisi, D. Di Girolamo, O. Tarquini, M. Colapietro, L. Barba, N. Demitri, A. Cassetta, *Dalton. Trans.* **2020**, *49*, 2616-2627.

[13] M. Aamir, Z. Hussain Shah, M. Sher, A. Iqbal, N. Revaprasadu, M. A. Malik, J. Akhtar, *Mater. Sci. Semicond. Process.* **2017**, *63*, 6-11.

[14] L. Malavasi, *in preparation*.

[15] A. Bala, V. Kumar, *J. Phys. Chem. C* **2019**, *123*, 25176-25184.

[16] I. Spanopoulos, I. Hadar, W. Ke, P. Guo, S. Sidhik, M. Kepenekian, J. Even, A. Mohite, R. D. Shcaller, M. G. Kanatzidis, *J. Am. Chem. Soc.* **2020**, *142*, 9028-9038.

[17] S. Cao, J. Low, J. Yu, M. Jaroniec, *Adv. Mater.* **2015**, *27*, 2150-2176.

[18] S. Ye, R. Wang, M.-Z. Wu, Y.-P. Yuan, *Appl. Surf. Sci.* **2015**, *358*, 15-27.

[19] Z. Zhao, Y. Sun, F. Dong, *Nanoscale* **2015**, *7*, 15.

[20] N. Fajrina, M. Tahir, *Int. J. Hydr. Energy* **2019**, *44*, 540-577.

[21] G. Liao, Y. Gong, L. Zhang, H. Gao, G.-J. Yang, B. Fang, *Energy Environ. Science* **2015**, *7*, 15.

[22] G. Thiele, B. R. Serr, *Zeit. Fur. Kristall.* **1996**, *211*, 47.

[23] F. Palazon, Y. El Ajjouri, P. Sebastia-Luna, S. Lauciello, L. Manna, H. J. Bolink, *J. Mater. Chem. C* **2019**, *7*, 11406-11410.

[24] L. Hou, Y. Zhu J. Zhu C. Li, *J. Phys. Chem. C* **2019**, 123, 31279.

[25] G. Beamson, D. Briggs - The Scienta ESCA300 Database Wiley Interscience **1992**, 278.

[26] Z.-A. Lan, G. Zhang, X. Wang, *Appl. Catal. B* **2016**, 192, 116.

[27] J. Zhou, M. Zhang, Y. Zhu, *PCCP* **2015**, *17*, 3647-3652.

[28] R. Zhang, X. Lu, L. Huang, Z. Ke, Y. Li, *J. Mater. Sci.: Mater. Elect.* **2017**, *28*, 8255-5265.

[29] K. Zhu, Y. Lv, W. Wang, C. Wang, S. Li, P. Wang, M. Zhang, A. Meng, Z. Li, *J. Alloy. Comp.* **2019**, *802*, 13-18.

[30] A. Speltini, A. Pisanu, A. Profumo, C. Milanese, L. Sangaletti, G. Drera, M. Patrini, M. Pentimalli, L. Malavasi, *RSC Adv.* **2018**, *8*, 39421.

[31] Z. Guo, F. Ambrosio, W. Chen, P. Gono, A. Pasquarello, *Chem. Mater*. **2018**, *30*, 1 94-111.

[32] F. Ambrosio, J. Wiktor, A. Pasquarello, *ACS Energy Lett*. **2018**, *3*, 4, 829-834.

[33] F. Ambrosio, G. Miceli, A. Pasquarello, *J. Chem. Phys*. **2015**, *143*, 244508.

[34] F. Ambrosio, Z. Guo, A. Pasquarello, *J. Phys. Chem. Lett*. **2018**, 9, 12, 3212-3216.

[35] Y. Q. Gao, Y. Georgievskii, R. A. Marcus, *J. Chem. Phys*. **2000**, *112*, 3358-3369.

[36] R.N. Sampaio, D.C. Grills, D.E. Polyansky, D.J. Szalda, E. Fujita, *J. Am. Chem. Soc*. **2020**, *142*, 2413-2428.